ACKNOWLEDGMENT

The authors thank Universiti Teknologi Malaysia (UTM) and Ministry of Higher Education (MOHE) Malaysia for supporting this research work under Research University Grant (RUG) Scheme grant no: 05J60 and grant no: 04H35, Fundamental Research Grant Scheme (FRGS) grant no: 4F317, and UTM Zamalah Fellowship.

REFERENCES

1. Y. Aoyagi, M. Takeuchi, K. Yoshida, M. Kurouchi, T. Araki, Y. Nanishi, H. Sugano, Y. Ahiko, and H. Nakamura, High-sensitivity ozone sensing using 280 nm deep ultraviolet light-emitting diode for detection of natural hazard ozone, J Environ Prot 3 (2012), 695–699.
2. M. Degner, N. Damaschke, H. Ewald, S. O'Keeffe, and E. Lewis, UV LED-based fiber coupled optical sensor for detection of ozone in the ppm and ppb range, In: Proceedings of IEEE Sensors Conference, 2009, pp. 95−99.
3. M. Degner, N. Damaschke, H. Ewald, and E. Lewis, High resolution LED-spectroscopy for sensor application in harsh environment: A sensor system based on LED-light sources and standard photodiode receiver is shown as an example of this sensor concept for in-situ gas measurements down to the ppb range, In: Proceedings of IEEE International Instrumentation and Measurement Technology Conference, 2010, pp. 1382−1386.
4. S. O'Keeffe, G. Dooly, C. Fitzpatrick, and E. Lewis, Optical fibre sensor for the measurement of ozone, J Phys Conf Ser 15 (2005), 213–218.
5. S. O'Keeffe, C. Fitzpatrick, and E. Lewis, An optical fibre based ultra violet and visible absorption spectroscopy system for ozone concentration monitoring, Sens Actuators B Chem 125 (2007), 372–378.
6. S. O'Keeffe, M. Ortoneda, J.D. Cullen, A. Shaw, D. Phipps, A.I. Al-Shamma'a, C. Fitzpatrick, and E. Lewis, Development of an optical fibre sensor system for online monitoring of microwave plasma UV and ozone generation system, In: Proceedings of IEEE Sensors Conference, 2008, pp. 454–457.
7. L.D. Maria, G. Rizzi, P. Serragli, R. Marini, and L. Fialdini, Optical sensor for ozone detection in medium voltage switchboard, In: Proceedings of IEEE Sensors Conference, 2008, pp. 1297−1300.
8. L.D. Maria and D. Bartalesi, A fiber-optic multisensor system for predischarges detection on electrical equipment, IEEE Sens J 12 (2012), 207–212.
9. I.M. Campbell, Energy and the atmosphere: A physical-chemical approach, 2nd ed., Wiley, New York, NY, 1986.
10. B.J. Clark, T. Frost, and M.A. Russell, Techniques in visible and ultraviolet spectrometry volume 4: UV spectroscopy, techniques, instrumentation, data handling, Chapman & Hall, London, UK, 1993.
11. H.K. Hughes, Beer's law and the optimum transmittance in absorption measurements, Appl Opt 2 (1963), 937–945.
12. K. Fuwa and B. L. Valle, The physical basis of analytical atomic absorption spectrometry. The pertinence of the Beer–Lambert law, Anal Chem 35 (1963), 942–946.
13. M. Yasin, S.W. Harun, C.F. Tan, S.W. Phang, and H. Ahmad, Fiber optic chemical sensor using fiber coupler probe based on intensity modulation for alcohol detection, Microwave Opt Technol Lett 53 (2011), 1935–1938.
14. Q. Yang, S.O. Pehkonen, and M.B. Ray, Performance evaluation of light emission models in light attenuating media, Ozone Sci Eng 27 (2005), 459–467.
15. R.J. Brock, A note on the Beer–Lambert law, Anal Chim Acta 27 (1962), 95–97.
16. M.L. Larsen and A.S. Clark, On the link between particle size and deviations from the Beer–Lambert–Bouguer law for direct transmission, J Quant Spectrosc Radiat Transf 133 (2014), 646–651.
17. L. Wind and W.W. Szymanski, Quantification of scattering corrections to the Beer–Lambert law for transmittance measurements in turbid media, Meas Sci Technol 13 (2002), 270–275.
18. E.C.Y. Inn and Y. Tanaka, Absorption coefficient of ozone in the ultraviolet and visible regions, J Opt Soc Am 43 (1953), 870–873.
19. J. Brion, A. Chakir, D. Daumont, J. Malicet, and C. Parisse, High-resolution laboratory absorption cross section of O3, Temperature effect, Chem Phys Lett 213 (1993), 610–612.
20. D. Daumont, J. Brion, J. Charbonnier, and J. Malicet, Ozone UV spectroscopy I: Absorption cross-sections at room temperature, J Atmos Chem 15 (1992), 145–155.
21. A.G. Hearn, The absorption of ozone in the ultra-violet and visible regions of the spectrum, Proc Phys Soc 78 (1961), 932–940.
22. J. Malicet, D. Daumont, J. Charbonnier, C. Parisse, A. Chakir, and J. Brion, Ozone UV spectroscopy, II. Absorption cross-sections and temperature dependence, J Atmos Chem 21 (1995), 263–273.
23. S. Voigt, J. Orphal, K. Bogumil, and J.P. Burrows, The temperature dependence (203–293 K) of the absorption cross sections of O3 in the 230–850 nm region measured by Fourier-transform spectroscopy, J Photochem Photobiol A Chem 143 (2001), 1–9.

AN INTEGRATED "SENSE-AND-COMMUNICATE" BROAD-/NARROW-BAND OPTICALLY CONTROLLED RECONFIGURABLE ANTENNA FOR COGNITIVE RADIO SYSTEMS

XiongYing Liu,[1] Yi Fan,[1] and Manos M. Tentzeris[2]
[1] School of Electronic and Information Engineering, South China University of Technology, Guangzhou 510640, China; Corresponding author: liuxy@scut.edu.cn
[2] School of Electrical and Computer Engineering, Georgia Institute of Technology, Atlanta, Georgia 30332

Received 13 September 2014

ABSTRACT: *An optically controlled reconfigurable antenna with operability in both wide and narrow bands is investigated for cognitive radio systems. The proposed antenna consists of a U-shaped patch for the spectrum sensing over a wide band and two open annuli for communication in narrow sub-bands within the frequency range of 3.1–10.6 GHz. The integration of narrow and wide bands devices makes the whole antenna structure compact with a dimension of 40 × 38.5 mm^2. With an inherent property of being electromagnetically transparency, four appropriately placed laser-controlled photoconductive silicon switches are adopted to achieve reconfigurable frequency characteristics in the four bands of 5.8–6.8, 6.7–7.3, 7.0–8.4, and 7.9–9.2 GHz with the reflection coefficient below -10 dB. The wide-narrowband antenna is fed by two coplanar waveguides with the isolation of $S_{21} < -15$ dB, effectively allowing the spectrum sensing and the communication to operate simultaneously. An antenna prototype has been fabricated, and close agreement is observed between the measured and simulated results.* © 2015 Wiley Periodicals, Inc. Microwave Opt Technol Lett 57:1016–1023, 2015; View this article online at wileyonlinelibrary.com. DOI 10.1002/mop.29004

Key words: *Frequency reconfigurable antenna; cognitive radio; optical control; photoconductive switches*

1. INTRODUCTION

With the increasing demand for wireless communications, the radio frequency spectrum has become a scarce resource. Nevertheless, some frequency bands in the spectrum, especially above 3 GHz, are partially unoccupied at most of the time [1]. However, according to the fixed spectrum access (FSA) policy [2], unauthorized users are not allowed to operate at the licensed spectrum. To improve the management and utilization of the radio spectrum, the Federal Communications Commission

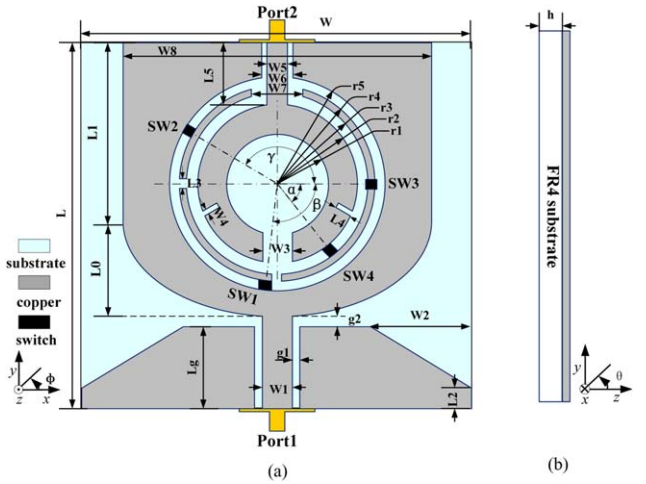

Figure 1 Configuration of the proposed antenna (a) top view and (b) side view. [Color figure can be viewed in the online issue, which is available at wileyonlinelibrary.com]

published a report [3], indicating that the spectrum utilization can be enhanced through the unlicensed users' accessing idle spectrum sub-bands while the authorized users do not occupy the licensed band. The cognitive radio (CR) technology is considered as one promising solution to help the unlicensed user search the idle spectrum sub-bands [4]. In a CR system, its operating parameters, such as communication frequencies, transmitting power and modulation modes, can be adjusted, hence sharing frequency bands and minimizing interference with conventional wireless systems. Especially, ultrawideband (UWB) antennas (i.e., "sensing antenna") can scan broad frequency range, effectively performing "spectrum sensing." When such an antenna detects an idle frequency band available, the integrated narrowband reconfigurable antenna (namely "communicating antenna") will switch to the corresponding unused band for communication [5].

Different types of designs integrating UWB and narrowband antennas have been proposed. Form literatures, mechanical switches and electrical devices, such as varactors and PIN diodes, have been incorporated in the reconfigurable antenna topologies. In [6], a combination of wideband and narrowband antennas, printed on the same side of a substrate, was investigated. The frequency reconfigurability is realized when five patches with different shapes are physically rotated via a stepper motor to touch the feeding line. In [7], a coplanar waveguide (CPW) fed UWB antenna which operates from 3.1 to 10.6 GHz was printed on the top side of a substrate, also acting as the ground for a planar inverted-F narrowband antenna that was etched on the reverse side. Using reconfigurable matching circuits, the narrowband antenna can work in three separate bands.

TABLE 1 Optimal Dimensions of the Proposed Antenna

Symbol	Value (mm)	Symbol	Value (mm)	Symbol	Value
W	40	W_7	4	L_0	10 mm
L	38.5	W_8	30	L_1	18 mm
Lg	10	r_1	4	L_2	3 mm
W_1	2	r_2	6.5	L_3	1 mm
W_2	10.5	r_3	7.5	L_4	1.5 mm
W_3	3	r_4	8.5	L_5	6 mm
W_4	0.5	r_5	9	α	54°
W_5	2	g_1	0.3	β	97°
W_6	2.5	g_2	0.5	γ	148°

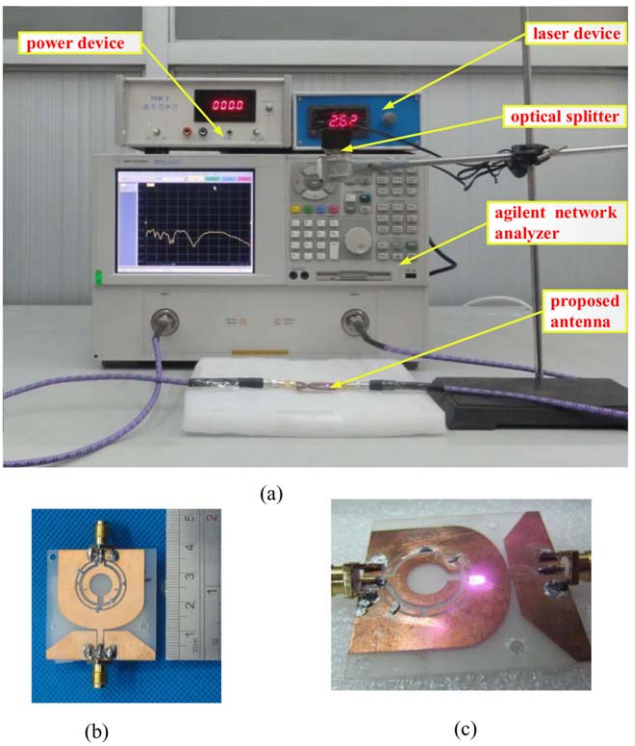

Figure 2 Photos of (a) measurement system, (b) fabricated widenarrowband antenna, and (c) front optical feeding. [Color figure can be viewed in the online issue, which is available at wileyonlinelibrary.com]

In [8], a slot resonator is embedded in the monopole patch to achieve a narrowband antenna. Over there, varactors with different biasing voltages are used to configure the impedance matching in each frequency band. While mechanical equipment may make the antenna bulky, and additional electrical biasing lines may have an adverse effect on the radiation of antenna.

In this study, we have presented an optically controlled integrated antenna topology with two CPW-feeding ports, effectively enhancing the operation speeds of spectrum sensing and communication. The proposed antenna is comprised of two parts. One part is an UWB, functioning as the spectrum sensor, while the other one acts as a reconfigurable narrowband resonator for communication, operating in one of four bands covering 5.8–6.8, 6.7–7.3, 7.0–8.4, and 7.9–9.2 GHz, respectively. The reconfigurable narrowband antenna is embedded in the middle blank space of the UWB monopole antenna, making the whole antenna compact with the dimension of 40 × 38.5 mm^2. The

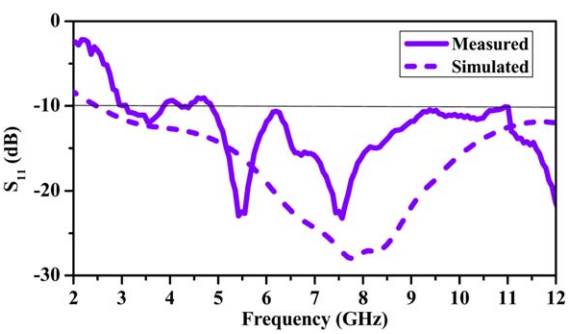

Figure 3 Measured and simulated values of the reflection coefficient of the UWB antenna. [Color figure can be viewed in the online issue, which is available at wileyonlinelibrary.com]

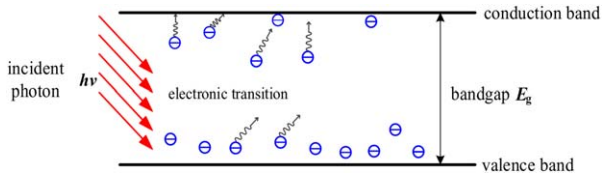

Figure 4 Plot of the photoemission process. [Color figure can be viewed in the online issue, which is available at wileyonlinelibrary.com]

reconfigurable antenna is controlled by four photoconductive silicon switches. Comparing with the electrical switches, the silicon switches have the advantage of electromagnetically transparency, hence, a significantly reduced electromagnetic impact on antenna radiation.

2. ANTENNA DESIGN

Figure 1 shows the proposed antenna, which is printed on a Flame Retardant-4 (FR4) substrate with relative permittivity

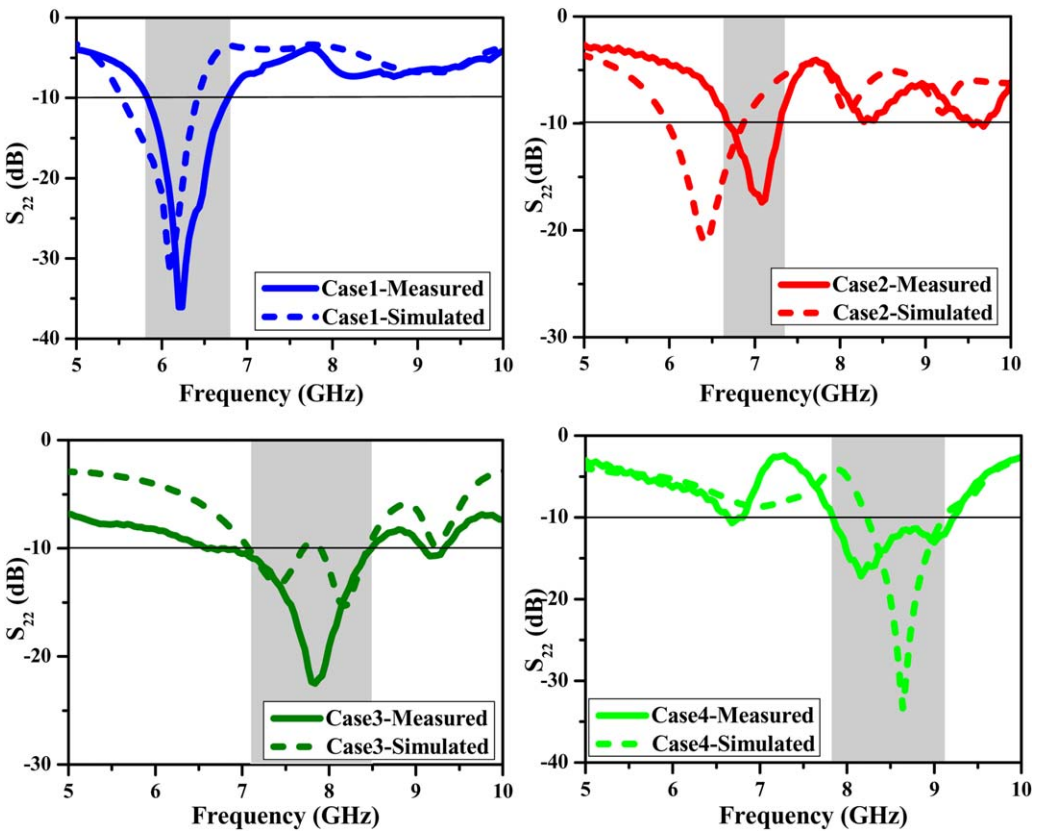

Figure 5 Measured and simulated values of the reflection coefficient of the narrowband antenna for four different cases. [Color figure can be viewed in the online issue, which is available at wileyonlinelibrary.com]

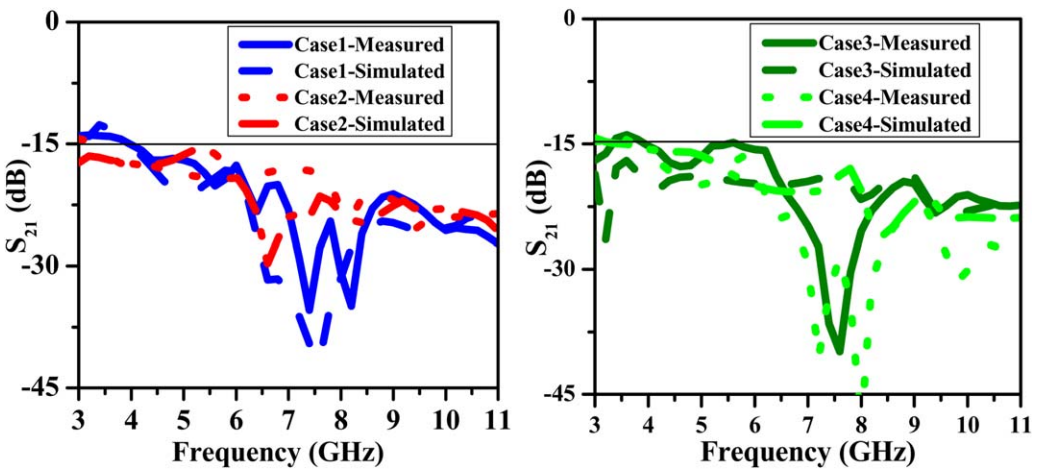

Figure 6 Measured and simulated values of the transmission coefficient for four different cases. [Color figure can be viewed in the online issue, which is available at wileyonlinelibrary.com]

Figure 7 Photo of the measurement setup of the radiation patterns. [Color figure can be viewed in the online issue, which is available at wileyonlinelibrary.com]

$\varepsilon_r = 4.4$, loss tangent tan $\delta = 0.02$, a thickness of $h = 0.5$ mm, and a dimension of 40 × 38.5 mm^2. The lower CPW fed U-shaped monopole antenna with a tapered ground, main for impedance matching, operates in the wide band from 3.1 to 10.6 GHz (i.e., UWB). The U-shaped patch also effectively functions as the ground for the upper CPW fed open-annulus narrowband antenna. Both the UWB and narrowband antennas are printed on the same side of the FR4 substrate, facilitating the connection/integration with other microwave devices and circuits. A coupling slender open ring is divided into four parts and embedded in the space between the UWB and narrowband antennas, enhancing the impedance matching over the different sub-bands.

To achieve frequency reconfigurable characteristics, four 1 × 1 × 0.4 mm^3 photoconductive switches (i.e., SW1 to SW4), shown with small dark blocks in the figure, are placed in the gaps of the proposed antenna. According to the effective length of current path on the slender ring, specific position of each switch is determined. When the light illuminates one of the switches, it turns "ON" and behaves as a short-circuiting conductor. Otherwise, it will be "OFF" and acts as an insulator. Two small symmetrical slots in the open-annulus strip are also cut to finely tune the input impedance of the narrowband antenna. Either the topology or the ground structure of inner narrowband antenna can be changed by combining specific slender ring parts with diverse switches states (namely "ON" or "OFF"), corresponding to different current paths in essence, so as to obtain four separately reconfigurable frequency bands. Here four reconfigurable frequency bands with S_{22} below −10 dB are achieved for CR communications. When only SW2 and SW4 are "ON" (Case1), the bandwidth is between 5.8 and 6.8 GHz. Once SW3 and SW4 are "ON" (Case 2), the antenna

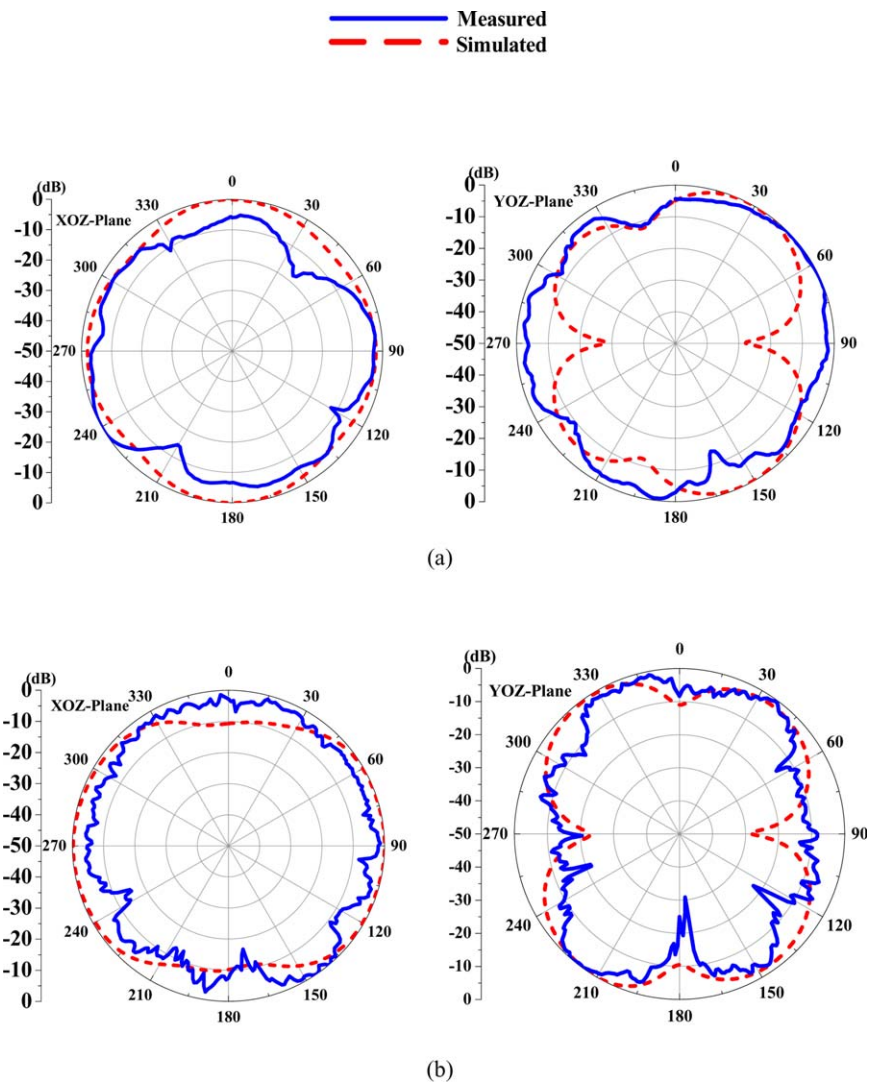

Figure 8 Measured and simulated radiation patterns of the UWB antenna at (a) 6.5GHz and (b) 8.5GHz. [Color figure can be viewed in the online issue, which is available at wileyonlinelibrary.com]

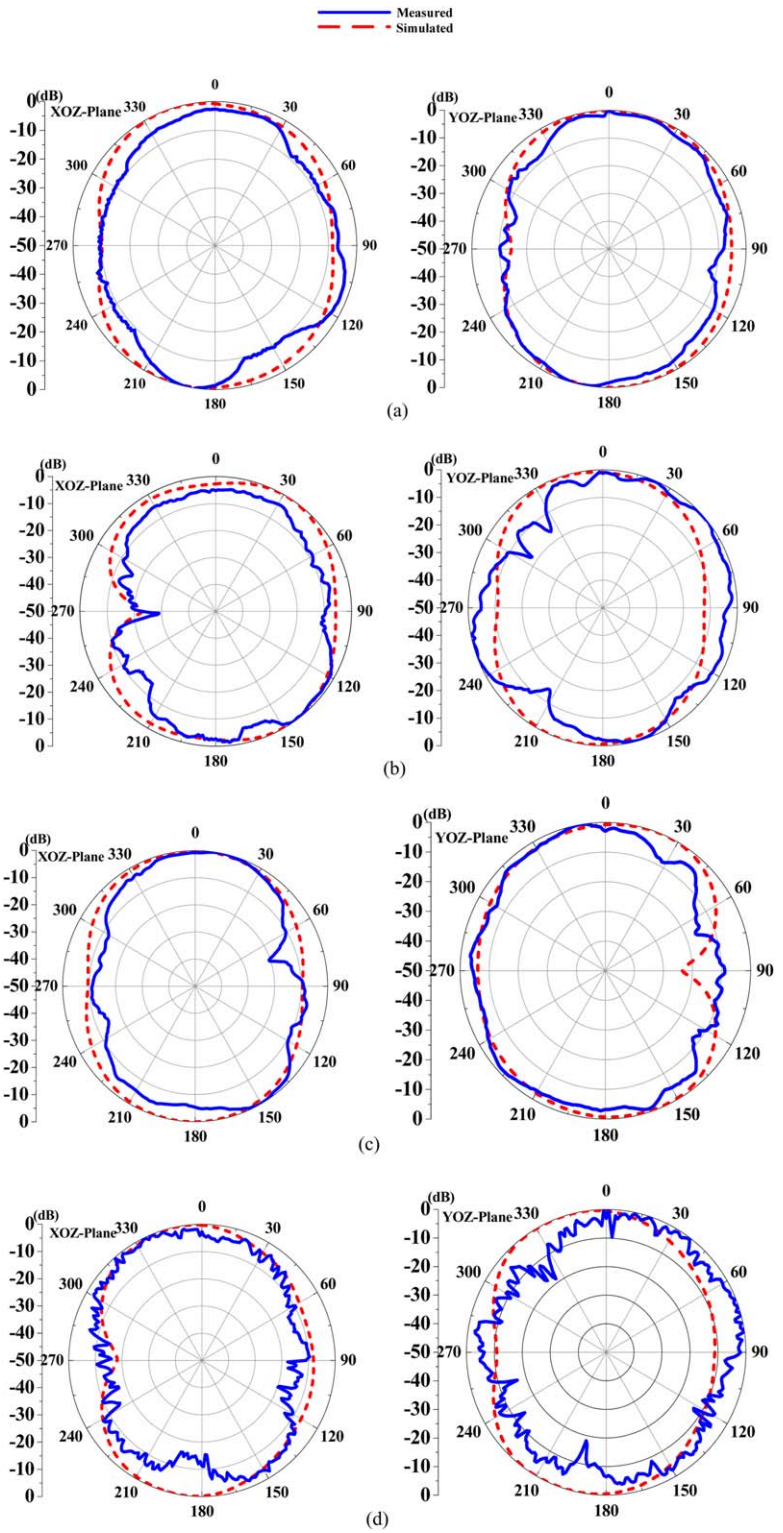

Figure 9 Measured and simulated radiation patterns of the narrowband antenna at (a) 6.2 GHz, (b) 6.9 GHz, (c) 7.8 GHz, and (d) 8.5GHz. [Color figure can be viewed in the online issue, which is available at wileyonlinelibrary.com]

shifts its band to 6.7–7.3 GHz. When only SW1 is activated (Case 3), 7.0–8.4 GHz band is covered. In Case 4, only SW2 is illuminated, 7.9–9.2 GHz band is realized.

During the design, the geometrical structure was first studied in detail by simulation with aid of ANSYS HFSS v.13, and then the prototype was fabricated and measured for verification. Through adjusting the geometric parameters of the proposed antenna, we finally obtained the optimal dimensions of the antenna, as listed in Table 1.

3. RESULTS AND DISCUSSION

The photographs of measurement devices, fabricated prototype, and front side laser-feeding are shown in Figure 2. The

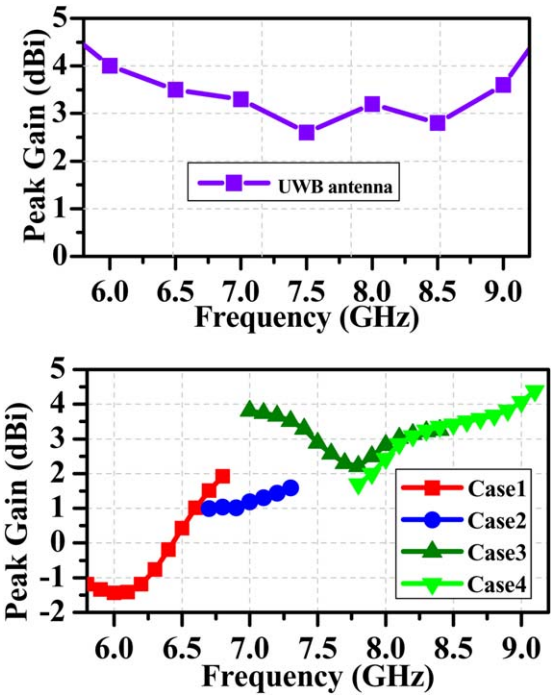

Figure 10 Measured peak gains of (a) the UWB antenna and (b) the narrowband antenna in different cases. [Color figure can be viewed in the online issue, which is available at wileyonlinelibrary.com]

reflection and transmission coefficients were measured using Agilent N5230A vector network analyzer. The simulated and measured reflection coefficients of the UWB antenna are depicted in Figure 3, validating the expected "spectrum sensing" band from 3.1 to 10.6 GHz with reflection coefficient of less than −10 dB.

3.1. Principle of the Photoconductive Silicon

According to the theory of internal photoelectric effects in semiconductors, when the energy of incident photon exceeds the bandgap energy E_g, the irradiated electrons in silicon will jump from the valence band to the conduction band, thereby making silicon behave as a conductor [9]. Figure 4 shows the principle of photoelectric effect. In this experimental measurement, an *n*-type silicon with high resistivity ($\rho = 2.5 \times 10^3$ Ω.cm) is implemented as the switching element. The bandgap energy of *n*-type silicon used in this work is about $E_g \approx 1.12$ eV. An 808 nm-wavelength laser is applied in this experiment and it can provide the energy of $hv = hc/\lambda_{laser} \approx 1.54$ eV $> E_g$, where "*h*" is the Planck constant, "*c*" is the speed of light and "*v*" represents the laser frequency.

3.2. Performance of the Reflection Coefficient in Four Cases

Figure 5 shows the reflection coefficients of the narrowband antenna, corresponding to different cases. The four reconfigurable bands are 5.8–6.8, 6.7–7.3, 7.0–8.4, and 7.9–9.2 GHz, which focus on the upper frequency sub-bands of UWB. The divergence between measured and simulated S parameters, especially in Case 2, is mainly due to laser power and switch manufacturing tolerances (e.g., the size of switch that has influence on the resistance).

3.3. Influence between Sensing- and Communicating-Antennas

In this design, the UWB and narrowband antennas were integrated together to reduce the overall size. Meanwhile, the advantage of the two feeding-port configuration with a reasonable isolation is that the sensing and communicating antennas can work at same time. That is to say, while the sensing antenna keeps searching the idle spectrum, the communicating antenna is ready to switch from a newly busy sub-band to an unused one.

To demonstrate the good isolation between the two antennas in the four cases of reconfigurability, the transmission coefficient between the spectrum sensing antenna with Port 1 and the communication antenna with Port 2 are simulated and measured. With reference to the Figure 6, the S_{21} is below −15 dB in the frequency range from 3.1 to 10.6 GHz and even reaches −20 dB over the band of 6-10 GHz.

3.4. Measurement of Far-Field Radiation Patterns

Due to the proposed antenna's operation in wireless frequencies with centimeter wavelength, we adopted an elevated outdoor far-field setup with virtually eliminated ground and stray wave

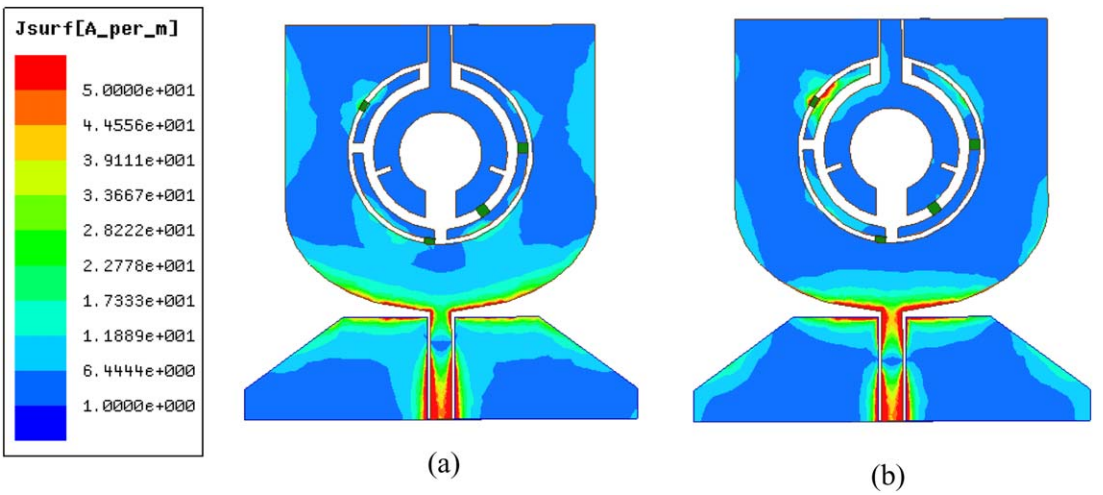

Figure 11 Surface current distribution on the UWB antenna at (a) 6.5 GHz and (b) 8.5 GHz. [Color figure can be viewed in the online issue, which is available at wileyonlinelibrary.com]

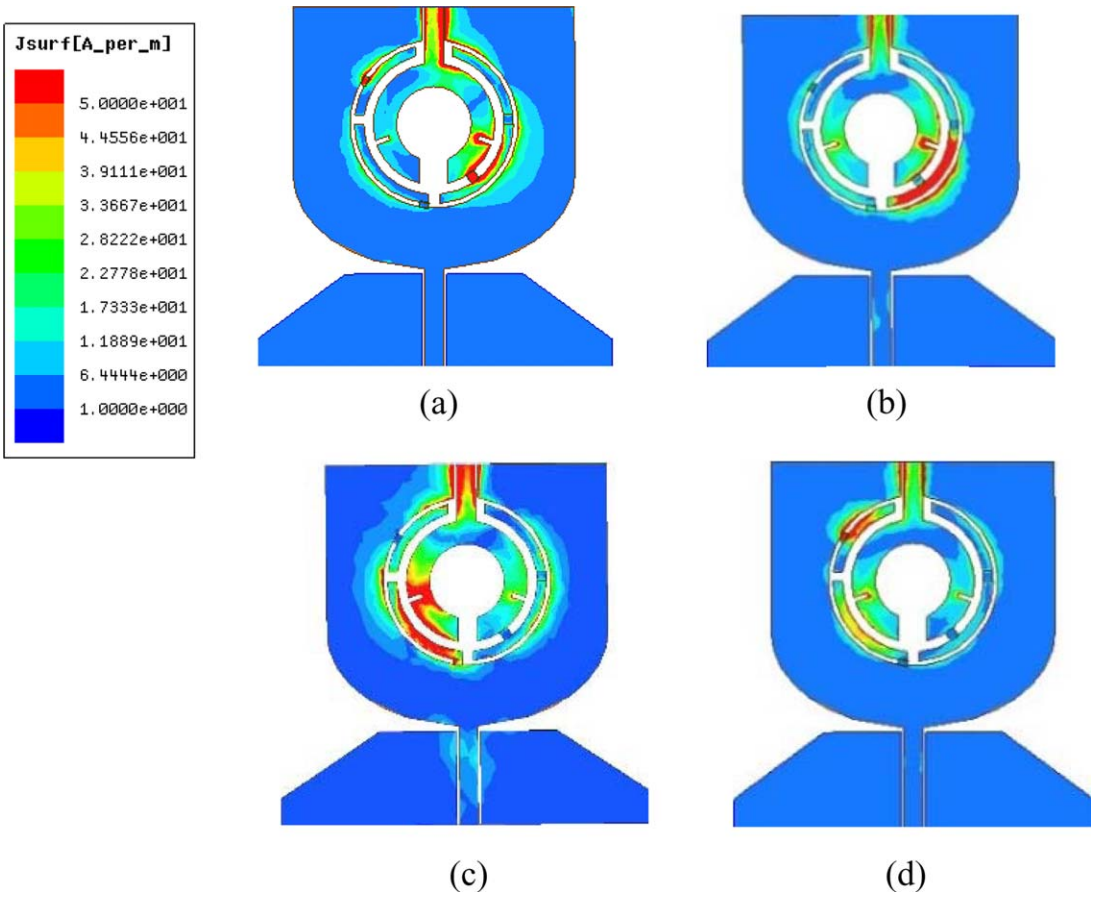

Figure 12 Surface current distribution on the narrowband antenna at (a) 6.2 GHz, (b) 6.9 GHz, (c) 7.8 GHz, and (d) 8.5 GHz. [Color figure can be viewed in the online issue, which is available at wileyonlinelibrary.com]

effects in the radiation pattern measurement. Figure 7 shows the detailed equipment configuration, located on the roof of an about 15-m high building. Figure 8 shows the measured and simulated radiation patterns of the UWB antenna (Port 1 excited, Port 2 terminated to a 50-Ω resistor) at 6.5 and 8.5 GHz, respectively, similar to those of the traditional UWB monopole antennas. The radiation patterns of the narrowband antenna (Port 2 excited, Port 1 = 50 Ω) in the four reconfigurable states are depicted in Figure 9. They are taken at 6.2 GHz (Case 1), 6.9 GHz (Case 2), 7.8 GHz (Case 3), and 8.5 GHz (Case 4), respectively. Some discrepancies are mainly attributed to the SMA connectors that are not considered into the HFSS simulations and the zero-angle calibration tolerance of the measurement system.

3.5. Analysis of Antenna's Gain

The measured maximum values of the proposed antenna's gains are illustrated in Figure 10. The gains of UWB antenna behave smooth in reconfigurable sub-bands. Considering the asymmetry switches and *ohmic* loss caused by the different current paths, the directivity and radiant efficiency of narrowband antenna are different in each case. Therefore, the gains vary at different reconfigurable frequency sub-bands.

3.6. Discussion on the Radiating Mechanism

To explain the radiating mechanism of the proposed antenna, the distribution of surface current on it is analyzed. The magnitude of the surface current on the UWB antenna at 6.5 and 8.5 GHz is shown in Figure 11. It is obvious that the UWB antenna has a dense surface current on the lower edge of the circumference and a weak current close to the centre of the topology. These properties can be efficiently utilized to embed the narrowband antenna within the UWB antenna with little effect on each other's radiation. In Figure 12, the current paths of narrowband antenna are varied by changing over the switches, thereby resulting in different operation frequency sub-bands

4. CONCLUSION

An integrated "sense and communicate" wide-/narrow-band optically reconfigurable antenna topology for CR systems has been presented. It consists of two substructures. One is a U-shaped monopole UWB antenna for spectrum sensing function and the other is an embedded open-annulus antenna with four photoconductive switches for communication at four reconfigurable subbands. The frequency reconfigurability is achieved through adjusting the structure of the narrowband subantenna with different combinations of "ON" and "OFF" switch states. The proposed antenna has two ports fed by individual CPWs. Therefore, sensing and communication can work independently, with less mutual influence. The proposed antenna was simulated and measured with good agreement, verifying its potential for an extensive use in CR communication systems.

ACKNOWLEDGMENT

This work was supported by the National Natural Science Foundation of China (61372008), in part by the Fundamental Research Funds for the Central Universities (2014ZZ0031), and

the National Engineering Technology Research Center for Mobile Ultrasonic Detection.

REFERENCES

1. N.K. Hoven, On the feasibility of cognitive radio, M.S. Thesis, University of California at Berkeley, Berkeley, CA, 2005.
2. European Regulatory Commission, The European table of frequency allocations and utilizations in the frequency range 9 KHz to 3000 GHz, CEPT/ERC Report, 2008.
3. FCC Spectrum Policy Task Force, Report of the spectrum Efficiency Working Group, 2002.
4. J. Mitola and G.Q. Maguire, Cognitive radiao: Making software radios more personal, IEEE Pers Commun 6 (1999), 13–18.
5. G.P. Jin, D.L. Zhang, and R.L. Li, Optically controlled reconfigurable antenna for cognitive radio applications, Electron Lett 47 (2011), 948–958.
6. Y. Tawk, J. Costantine, K. Avery, and C.G. Christodoulou, Implementation of a cognitive radio front-end using rotatable controlled reconfigurable antennas, IEEE Trans Antennas Propag 59 (2012), 1773–1778.
7. E. Ebrahimi, J.R. Kelly, and P.S. Hall, Integrated wide-narrowband antenna for multi-standard radio, IEEE Trans Antennas Propag 59 (2012), 2628–2635.
8. G. Augustin, T.A. Denidni, An integrated ultra wideband/narrow band antenna in uniplanar configuration for cognitive radio systems, IEEE Trans Antennas Propag 60 (2012), 5479–5484.
9. Photoelectric effect. Available at: http://en.wikipedia.org/wiki/Photoelectric_effect.

ERRATUM FOR: CHARACTERISTICS OF OPTICAL GLASS PLATE REFRACTIVE INDEX SENSOR BASED ON SURFACE PLASMON RESONANCE

Cien-Jen Tang,[1] Chen-Hung Lin,[2] Li-Jen Hsiao,[2] Wei-Tsung Chen,[1] Cheng-Chung Jaing,[1] and Hoang Yan Lin[2]
[1] Department of Opto-Electronic System Engineering, Minghsin, University of Science and Technology, No.1, Xinxing Rd., Xinfeng, Hsinchu 30401, Taiwan
[2] Department of Electrical Engineering, Graduated Institute of Photonics and Optoelectronics, National Taiwan University, No.1, Sec.4, Roosevelt Rd., Taipei 10617, Taiwan; Corresponding author: d94941010@ntu.edu.tw

Received 1 May 2014

In the above-mentioned article, which appeared in Microwave and Optical Technology Letters, © 2014 Wiley Periodicals, Inc. Microwave Opt Technol Lett 56:3009–3012, 2014; View this article online at wileyonlinelibrary.com. DOI 10.1002/mop.28757. © 2015 Wiley Periodicals, Inc. Microwave Opt Technol Lett 57:1023, 2015; View this article online at wileyonlinelibrary.com. DOI:10.1002/mop.29006, the first author's name was incorrectly shown. The correct name is listed below:

Chien-Jen Tang

The authors regret any confusion that resulted from this error.